

Compact 3D Gaussian Splatting For Dense Visual SLAM

Tianchen Deng¹, Yaohui Chen¹, Leyan Zhang¹, Jianfei Yang², Shenghai Yuan², Danwei Wang², and Weidong Chen¹

¹ Shanghai Jiao Tong University

² Nanyang Technological University

Abstract. Recent work has shown that 3D Gaussian-based SLAM enables high-quality reconstruction, accurate pose estimation, and real-time rendering of scenes. However, these approaches are built on a tremendous number of redundant 3D Gaussian ellipsoids, leading to high memory and storage costs, and slow training speed. To address the limitation, we propose a compact 3D Gaussian Splatting SLAM system that reduces the number and the parameter size of Gaussian ellipsoids. A sliding window-based masking strategy is first proposed to reduce the redundant ellipsoids. Then we observe that the covariance matrix (geometry) of most 3D Gaussian ellipsoids are extremely similar, which motivates a novel geometry codebook to compress 3D Gaussian geometric attributes, i.e., the parameters. Robust and accurate pose estimation is achieved by a global bundle adjustment method with reprojection loss. Extensive experiments demonstrate that our method achieves faster training and rendering speed while maintaining the state-of-the-art (SOTA) quality of the scene representation.

1 Introduction

Simultaneous localization and mapping (SLAM) has been a fundamental computer vision problem with wide applications such as autonomous driving, robotics, and virtual/augmented reality [7, 28]. Several traditional methods, including ORBSLAM [24, 25], VINS [27], etc. [6, 37, 38], have been introduced over the years, representing scenes with sparse point cloud maps. However, due to the sparse nature of the point cloud, it proves ineffective for navigation or other purposes. Attention has turned to dense scene reconstruction, exemplified by DTAM [26], Kintinuous [35], and ElasticFusion [36]. However, their accuracy remains unsatisfactory due to high memory costs, slow processing speeds, and other real-time running limitations.

Nowadays, with the proposal of Neural Radiance Fields (NeRF) [22], there are many following works on different areas [4]. Many works focus on combining implicit scene representation with SLAM systems. iMAP [32] is the first method to use a single MLP to represent the scene. NICE-SLAM [45], ESLAM [11], Co-SLAM [34], and PLGSLAM [5] further improve the scene representation with

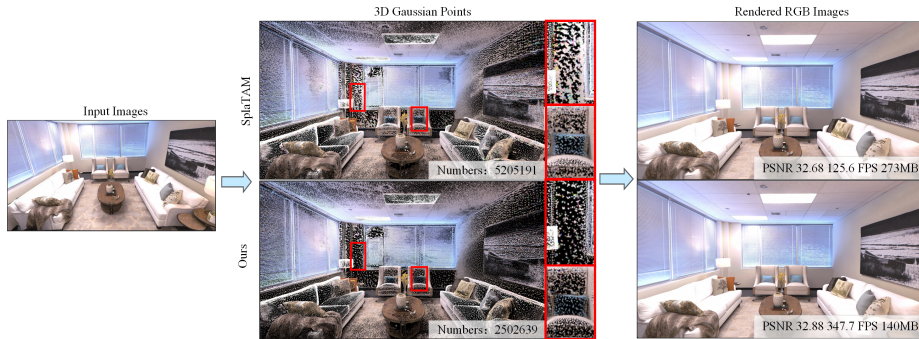


Fig. 1: Our framework minimizes storage and accelerates rendering while maintaining the SOTA image reconstruction performance. The proposed framework eliminates unnecessary 3D Gaussian ellipsoids without affecting performance. We highlight and enlarge some areas to show the significant reduction of 3D Gaussian points.

the hybrid feature grids, axis-aligned feature planes, joint coordinate-parametric encoding, and progressive scene representation. To further improve the accuracy of rendering, recent methods have started to explore 3D Gaussian Splatting(GS) [13] integration with SLAM, such as SplatTAM [12], GS-SLAM [39], etc [21, 42]. GS-based SLAM methods leverage a point-based representation associated with 3D Gaussian attributes and adopt the rasterization pipeline to render the images, achieving fast rendering speed and promising image quality. However, the original GS-based scene representation entails a substantial number of 3D Gaussian ellipsoids to maintain high-fidelity reconstruction, leading to high memory usage and storage requirements. GS-based SLAM systems usually need more than 500MB to represent a small room-sized scene. Moreover, the running speed of GS-based SLAM systems is significantly slower than NeRF-based methods, which hinders practical deployment, especially on resource-constrained devices.

To this end, we propose a compact 3D Gaussian scene representation method to address the critical high memory demand and slow training speed issue in GS-based SLAM systems. Our method notably enhances storage efficiency while delivering high-quality reconstruction, fast training speed, and real-time rendering capabilities. First, we design a novel sliding window-based online masking method to remove the millions of redundant and unnecessary 3D Gaussian ellipsoids created during the SLAM system operation. With the proposed masking method, a compact 3D Gaussian scene representation is learned, achieving faster rendering speed and efficient memory usage since the computational complexity is linearly proportional to the number of 3D Gaussian points.

Second, we observe that the majority of Gaussian points exhibit similar geometry information in scale and rotation attributes. To this end, a codebook-based method is designed to compress the geometry of each Gaussian point. It learns to find the similarities and geometry shared across the scene. We only store the codebook index for each 3D Gaussian ellipsoid, obtaining compact scene representation.

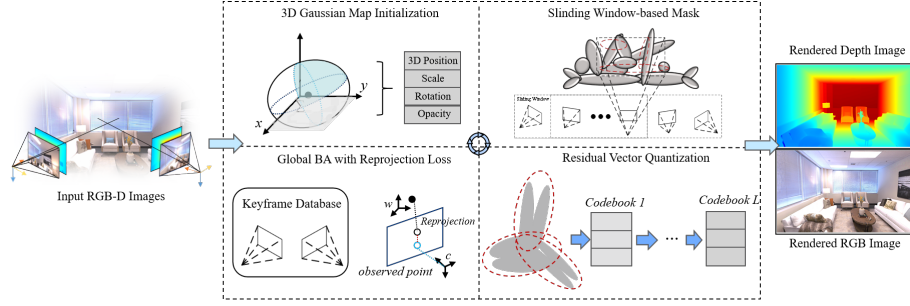


Fig. 2: The pipeline of our GS-based SLAM system. The input of our system is the current RGB-D frame. We start the SLAM system by initializing the 3D Gaussian map construct. Then, we update our 3D Gaussian map by adding new Gaussians and using the learnable mask to reduce the redundant 3D Gaussian ellipsoids. We incorporate a codebook-based vector quantization method to compress the scene representation. For camera tracking, we maintain a global keyframe database for global BA and use reprojection loss for robust pose estimation.

Third, the camera tracking accuracy of GS-based SLAM is relatively low compared with other SLAM systems. A global BA method with reprojection loss is proposed to achieve robust and accurate pose estimation. Our method maintains a global keyframe database and performs bundle adjustment with all the historical observations, which can effectively eliminate the cumulative error.

Overall, our contributions are shown as follows:

- We propose a novel GS-based SLAM system with compact Gaussian scene representation, achieving fast training and rendering speed, accurate pose estimation, and significantly enhancing storage efficiency.
- A novel sliding window-based online masking method is proposed to remove the number of redundant Gaussian ellipsoids while achieving high-fidelity performance during training.
- We observe and analyze the geometry similarities of 3D Gaussian ellipsoids and propose a codebook-based method to efficiently restore the geometry of each Gaussian point during the SLAM system operation. A keyframe-based global BA method with reprojection loss is proposed to improve the relative low performance of camera tracking.
- We conduct comprehensive experiments on different datasets and achieve nearly 176% increase in rendering speed and over $1.97\times$ compression on memory usage.

2 Related Work

Dense Visual SLAM and Localization. SLAM [2, 19] and localization [20] has become an active field for the past two decades. DTAM [26] is the first method to achieve dense scene reconstruction. Kinectfusion [10] uses projective iterative-closest-point (ICP) for camera tracking. Some learning-based methods

integrate traditional geometry frameworks with deep learning networks for accurate camera tracking and mapping, such as DROID-SLAM [33].

NeRF-based SLAM. With the proposal of Neural radiance fields (NeRF) [22], many researchers explore taking advantage of the implicit method into SLAM systems. iMAP [32] is the first method to use a single multi-layer perceptron (MLP) to represent the scene, and NICE-SLAM [45] uses learnable hierarchical feature grids. Vox-Fusion [40] employs octree architecture for dynamic map scalability. ESLAM [11] and Co-SLAM [34] further improve the scene representation with tri-planes and joint coordinate-parametric encoding. [17, 18, 44] use semantic feature embedding to improve scene representation. Point-SLAM [29] uses neural point clouds for the scene representation. Instead of representing maps with neural implicit features, our method utilizes the explicit 3D Gaussian representation, which can significantly improve the rendering speed using splatting-based rasterization.

GS-based SLAM. Recently, 3D Gaussian Splatting (3DGS) [13] using 3D Gaussians as primitives for real-time neural rendering. 3DGS utilizes highly optimized custom CUDA kernels and novel algorithmic approaches, which achieve significant improvements in rendering speed without sacrificing image quality. SplaTAM [12], GS-SLAM [39], Gaussian-SLAM [42], Gaussian Splatting SLAM [21] are the pioneer works that successfully combine the advantages of 3D Gaussian Splatting with SLAM. These methods achieve fast rendering speed and high-fidelity reconstruction performance. However, the training speed is relatively slow, which is crucial for SLAM as it is an online operation system. Memory and storage usage are also heavy, which makes them difficult to use in real-world scenarios and with handheld devices.

3 Method

The pipeline of our system is shown in Fig. 2. The input of our system is sequential RGB-D frames $\{I_i, D_i\}_{i=1}^M$ with known camera intrinsic $K \in R_{3 \times 3}$. Our system simultaneously reconstructs a dense scene map and estimates camera poses $\{R_i | t_i\}_{i=1}^M$. For the mapping thread, a compact 3D Gaussian scene representation (Sec. 3.1) is designed to represent the environments with sliding window-based masks (Sec. 3.2) and geometry codebook (Sec. 3.3). For the camera tracking thread, a global bundle adjustment method (Sec. 3.4) is designed for robust and accurate pose estimation. The network is incrementally updated with the SLAM system operation.

3.1 3D Gaussian Scene Representation

Inspired by [13], We represent the entire scene as a set of 3D Gaussian ellipsoids. Each 3D Gaussian is associated with 3D attributes (positions, opacity, scale, and rotation). Our Gaussian ellipsoids are defined by a full 3D covariance matrix Σ defined in world space (normalized):

$$f(\mathbf{x}) = \sigma e^{-\frac{1}{2}(\mathbf{x})^T \Sigma^{-1}(\mathbf{x})}, \quad \Sigma = R S S^T R^T \quad (1)$$

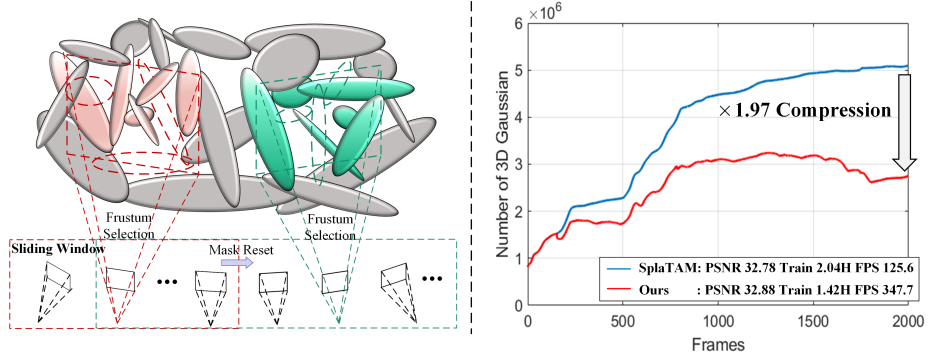


Fig. 3: The left figure shows the learnable mask strategy. We perform frustum selection and sliding window reset to remove redundant Gaussian ellipsoids while maintaining the reconstruction accuracy efficiently. The dashed lines represent the removed 3D Gaussian ellipsoids. The right figure shows the varying count of Gaussian ellipsoids during the SLAM system operation. These two curves show the distinction between our system with and without masks. Our mask strategy achieves **1.97** \times compression on the number of 3D Gaussians.

where $\alpha \in [0, 1]$ is the opacity value. \mathbf{S} is the scaling matrix, and \mathbf{R} is the rotation matrix.

Then we use the 3D Gaussian ellipsoids to render 2D images with the technique of splatting [14, 41]. Then we can formulate the covariance matrix Σ' in camera coordinates:

$$\Sigma' = \mathbf{J} \mathbf{W} \Sigma \mathbf{W}^T \mathbf{J}^T \quad (2)$$

where \mathbf{W} denotes the view direction, \mathbf{J} denotes the projection transformation matrix. For each pixel p , the color and opacity of all Gaussian ellipsoids are computed and blended using this formula:

$$C(p) = \sum_{i \in N} c_i f_i(p) \prod_{j=1}^{i-1} (1 - f_j(p)) \quad (3)$$

where c_i denotes the color of Gaussian ellipsoids. We also propose a similar depth rendering formula:

$$D(p) = \sum_{i=1}^n d_i f_i(\mathbf{p}) \prod_{j=1}^{i-1} (1 - f_j(p)) \quad (4)$$

We also render a silhouette image to determine visibility:

$$S(p) = \sum_{i=1}^n f_i(p) \prod_{j=1}^{i-1} (1 - f_j(p)) \quad (5)$$

3.2 Sliding Window-based Mask

The existing GS-based SLAM systems, such as SplaTAM [12] and GS-SLAM [39], directly use the original 3DGS for scene representation, achieving promising image quality. However, we observe that the 3DGS creates a number of redundant 3D Gaussian ellipsoids with the SLAM system operation ($\times 1.52$ Gaussian ellipsoids show similar performance in Fig. 3), while both of them fail to discover this. This finally results in poor performance in training speed, memory, and storage usage, which is crucial for online SLAM systems. Some methods [9, 16, 23] propose novel Gaussian pruning and self-organizing methods to compact the 3DGS attributes. However, all of these strategies are not suitable for GS-based SLAM systems as they have to obtain all the images, pose, and the corresponding point cloud at the beginning, while SLAM systems are incrementally optimized.

To this end, we propose a learnable sliding window-based mask strategy to remove the redundant 3D Gaussian ellipsoids with the SLAM system operation. Compared to the original densification method, which only considers the opacity, our method takes into account both the volume V and opacity $o \in [0, 1]$ of Gaussian ellipsoids. The volume calculation is $V = \frac{4}{3}\pi abc$, where abc are the three dimensions of the scale \mathbf{S} . We introduce a learnable mask parameter $m \in R^N$ and a corresponding binary mask $M \in \{0, 1\}^N$, N is the number of Gaussian ellipsoids.

$$M_n = \text{sg}(\mathbb{I}[\text{Sig}(m_n) > \epsilon] - \text{Sig}(m_n)) + \text{Sig}(m_n) \quad (6)$$

$$\hat{\mathbf{S}}_n = M_n \mathbf{S}_n, \quad \hat{o}_n = M_n o_n \quad (7)$$

where n is the index of the Gaussian ellipsoids, ϵ denotes the mask threshold. Inspired by [1], we employ the stop gradient operator $\text{sg}(\cdot)$ to calculate gradients from binary masks. \mathbb{I} and $\text{Sig}(\cdot)$ denote the indicator and sigmoid function. This formulation of mask strategy allows us to effectively combine the influence of volume and opacity of Gaussian ellipsoids. We formulate the loss function L_m of our mask:

$$L_m = \frac{1}{N} \sum_{n=1}^N \text{Sig}(m_n) \quad (8)$$

In order to better fit the online updating SLAM systems, we further improve the masking strategy by adding frustum culling and sliding window-based reset strategy, shown in Fig. 3. Our frustum culling strategy allows us to optimize only the mask within the current viewing frustum while keeping the rest of the 3D Gaussian ellipsoids fixed. It will not only preserve the previously reconstructed geometry but also significantly reduce the number of parameters during optimization. Different from the original densification strategy performed on every frame, we only perform mask on the keyframe (each k^{th} frame) for efficiency and accuracy. We maintain a local sliding window and perform sliding window reset to avoid the continuous optimization and accumulated gradient of masks which will ultimately eliminate all Gaussian ellipsoids. The sliding window consists of the current frame, the most relevant keyframe, and $n - 2$ previous keyframes,

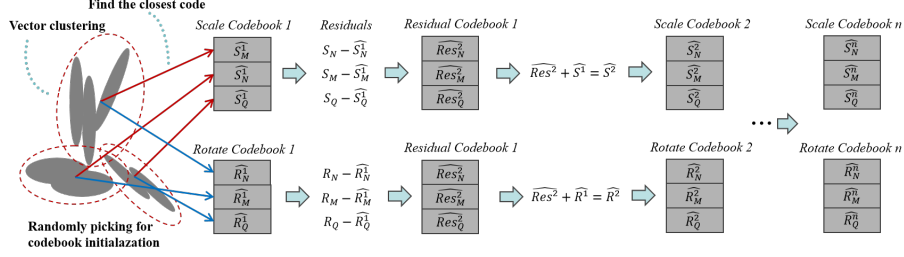


Fig. 4: The R-VQ process to represent the scale and rotation of Gaussian ellipsoids. In the first stage, we cluster the scale and rotation vectors and randomly select codebook initialization with the closest code. In the subsequent stage, the residual between the original vector and the result from the first stage is stored in another codebook. This iterative process continues through to the ultimate stage, at which point, the collectively chosen indices and codebook from each stage provide a representation of the original vector.

which have the highest overlap with the current frame. Overlap is evaluated by analyzing the point cloud of the current frame’s depth map and tallying points within the frustum of each keyframe. This can also ensure the consistency of the mask within the local sliding window. This approach allows us to continuously mask out unnecessary Gaussians during online SLAM system operation, effectively reducing computation overhead and ensuring efficient memory usage on GPU.

3.3 Geometry Codebook

In this section, we analyze and observe the geometry similarities of the Gaussian ellipsoids created by SLAM systems. Then, we propose a learnable codebook and employ a residual vector quantization method to reduce computational complexity and memory usage and further improve the training and rendering speed.

For the GS-based SLAM system, a scene is composed of a number of small Gaussian ellipsoids with 3D geometry attributes (scale and rotation matrix \mathbf{S}, \mathbf{R}). Consider that the 3D Gaussian ellipsoids G_1, G_2 conform to an unbiased Gaussian distribution $\mathcal{N}(0, \Sigma_1), \mathcal{N}(0, \Sigma_2)$, we adopt the Kullback-Leibler divergence [15] to analysis the geometry similarities of 3D Gaussian ellipsoids:

$$D_{KL} = \frac{1}{2p} \text{tr}(\Sigma_1^{-1} \Sigma_2) - \frac{1}{2} + \frac{1}{2p} \ln \det(\Sigma_1^{-1} \Sigma_2) \quad (9)$$

where p is the dimension of the covariance matrix. We conduct extensive experiments and present our results on Tab. 1 and Fig. 5. We can see that the percentage of 3D Gaussian ellipsoids is significantly elevated in a small range of KL divergence, which demonstrates the similarities of the 3D Gaussian ellipsoids shared across the scene. Our experiments also show that the similarities of 3D Gaussians of the GS-based SLAM system are greater than the original 3DGS. This is probably due to the online optimization strategy that the SLAM system

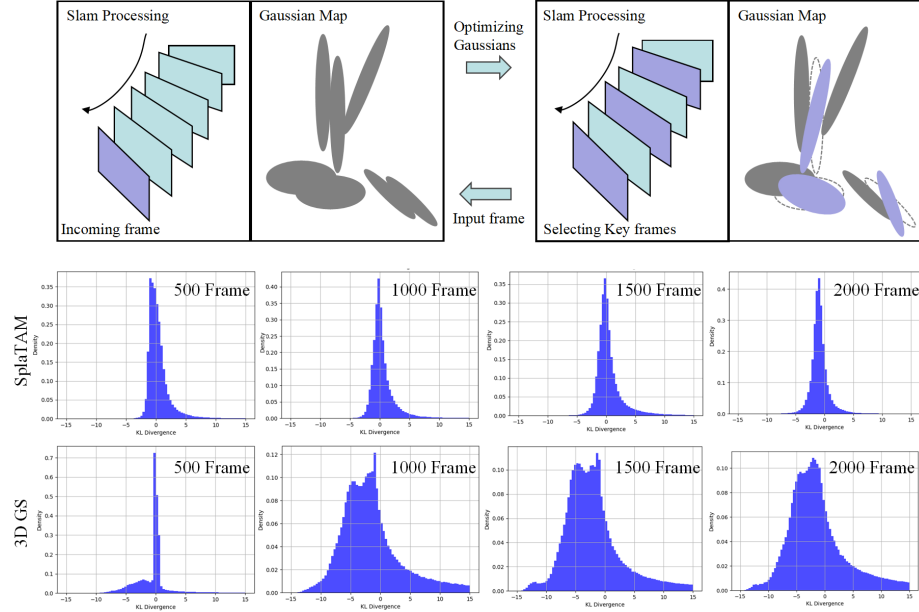


Fig. 5: The KL divergence distribution of the Gaussian ellipsoids with the online training of the SLAM system on different time steps (500, 1000, 1500, 2000). We can observe that the similarity in geometry consistently remains at a high level of GS-based SLAM system.

only uses the current frame and history keyframes to optimize the 3D Gaussian attributes, which will exacerbate the geometry similarity. Based on the similarity, we propose a learnable codebook to compress the geometry attributes (scale and rotation), shown in Fig. 4. Inspired by SoundStream [43] and Encodec [8], we incorporate the residual vector quantization (R-VQ) to compress the scale and rotation. It cascades L stages of VQ and is formulated as follows:

$$\begin{aligned} \hat{S}_n^l &= \sum_{k=1}^l \mathcal{C}^k [i_n^k], \quad l \in \{1, \dots, L\}, \\ i_n^l &= \underset{k}{\operatorname{argmin}} \left\| \mathcal{C}^l[k] - \left(S_n - \hat{S}_n^{l-1} \right) \right\|_2^2, \quad \hat{S}_n^0 = \vec{0} \end{aligned} \quad (10)$$

where $S \in \mathcal{R}^{N \times 4}$ is the scale vector, $\hat{S}^l \in \mathcal{R}^{N \times 4}$ is the output scale vector after l stages quantization. n denotes the index of the Gaussian ellipsoids. \mathcal{C}^l denotes the codebook at the stage l . \mathcal{C}^l represents the vector at index i of the codebook \mathcal{C} . The formulation of the rotation vector is the same. Then, the loss function is defined as:

$$L_r = \frac{1}{NP} \sum_{k=1}^L \sum_{n=1}^N \left\| \operatorname{sg} \left[S_n - \hat{S}_n^{k-1} \right] - \mathcal{C}^k [i_n^k] \right\|_2^2 \quad (11)$$

where P is the size of codebook, $sg[\cdot]$ is the stop gradient operator. After this, we can only store the codebook compressed scale and rotation vector, which can significantly reduce storage and memory usage.

Table 1: The KL divergence analysis of GS-based SLAM and original 3DGS.

SpliTAM [12]		3DGS [13]	
Range	Percentage	Range	Percentage
(-2.5%,2.5%)	87.67%	(-2.5%,2.5%)	20.07%
(-5.0%,5.0%)	97.86%	(-5.0%,5.0%)	37.04%
(-7.5%,7.5%)	99.16%	(-7.5%,7.5%)	47.69%
(-10.0%,10.0%)	99.52%	(-10.0%,10.0%)	52.16%

3.4 Tracking and Global Bundle Adjustment

Our tracking and bundle adjustment are performed via minimizing our objective functions. The camera pose is initialized for a new time step by a constant velocity forward projection of the pose parameters. The color and depth loss is defined as:

$$\mathcal{L}_c = \frac{1}{N} \sum_{i=1}^N \left(\hat{\mathbf{C}}_i - \mathbf{C}_i \right)^2, \quad \mathcal{L}_d = \frac{1}{|R_i|} \sum_{i \in R_i} \left(\hat{\mathbf{D}}_i - \mathbf{D}_i \right)^2 \quad (12)$$

where R_i is the set of rays that have a valid depth observation. The reprojection error is common in traditional SLAM methods based on sparse point clouds [25]. Since 3D Gaussian is also based on a point cloud representation, we introduce this loss for the first time to improve the scene’s geometric representation and consistency further. We formulate reprojection errors with SIFT features:

$$\mathcal{L}_{re} = \sum_{i=1}^n \left\| (u_{i'}, v_{i'}) - \Pi(R_{i \rightarrow i'} P_i + t_{i \rightarrow i'}) \right\| \quad (13)$$

where $\Pi(R_{i \rightarrow i'} P_i + t_{i \rightarrow i'})$ represents the reprojection of 3D point P_i to the corresponding pixel $(u_{i'}, v_{i'})$ in image i' . The tracking loss is formulated as follows:

$$L_t = \sum_{\mathbf{p}} (S(\mathbf{p}) > 0.99) (\mathcal{L}_c + \lambda_1 \mathcal{L}_d + \lambda_2 \mathcal{L}_{re}) \quad (14)$$

We use the rendered visibility silhouette to select the well-optimized pixels for camera tracking, which can improve the tracking accuracy for the new frames.

Global Bundle Adjustment. For global consistency and accuracy, our system maintains a significantly larger global keyframe database than other GS-based SLAM systems. We randomly sample a total number of N rays from our global keyframe database to optimize our scene representation as well as camera poses. This phase optimizes a loss similar to tracking loss, and we also add an SSIM loss to RGB rendering. The global bundle adjustment is performed to optimize the scene representation with the camera pose. Our global BA method can effectively reduce cumulative errors and enhance the robustness of pose estimation, especially for long sequences and large scenes.

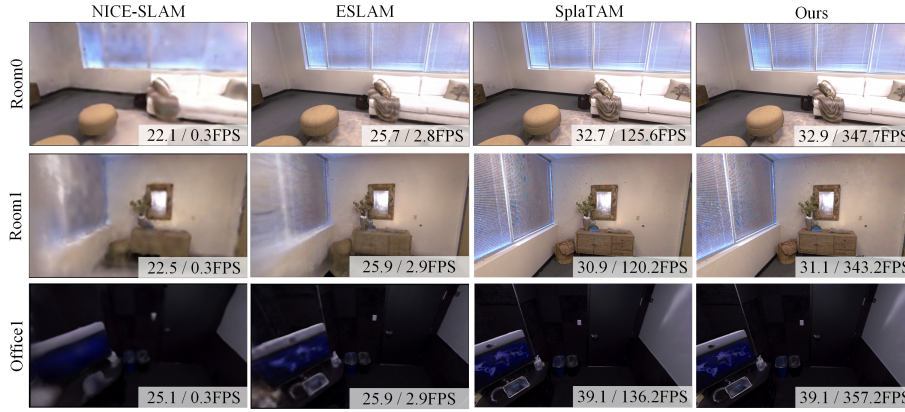


Fig. 6: The rendering visualization results on the Replica dataset [30] of the proposed GS-based SLAM system compared with other SOTA methods. We present the rendering PSNR and FPS on the image. Our method can achieve faster rendering speed and high-quality image reconstruction performance compared with other methods.

Table 2: Camera tracking results on Replica dataset [30]. We use the ATE RMSE $\downarrow [cm]$ as the metric and compare it with other SOTA methods.

Methods	Avg.	R0	R1	R2	Of0	Of1	Of2	Of3	Of4
Vox-Fusion [40]	3.09	1.37	4.70	1.47	8.48	2.04	2.58	1.11	2.94
NICE-SLAM [45]	1.06	0.97	1.31	1.07	0.88	1.00	1.06	1.10	1.13
ESLAM [11]	0.63	0.71	0.70	0.52	0.57	0.55	0.58	0.72	0.63
Co-SLAM [34]	0.78	0.61	0.79	0.96	0.54	0.52	1.13	0.97	0.74
Point-SLAM [29]	0.52	0.61	0.41	0.37	0.38	0.48	0.54	0.69	0.72
SplatAM [12]	0.36	0.31	0.40	0.29	0.47	0.27	0.29	0.32	0.55
Ours	0.33	0.27	0.38	0.25	0.44	0.27	0.27	0.29	0.50

4 Experiments

Datasets and Evaluation Metrics. We evaluate our method on various datasets: Replica [30], Scannet [3], and TUM-RGBD [31], following the settings from SplatAM [12]. The replica is a synthetic dataset, and we select eight small room scene sequences for evaluation. We select six real-world scenes from the ScanNet [3] dataset for relatively large-scale indoor scenes. We also select five scenes from the TUM RGB-D [31] dataset as it is a common dataset for evaluating camera tracking accuracy. We follow the evaluation metrics from SplatAM [12]. We use PSNR, SSIM, and LPIPS to measure rendering performance. For camera pose estimation, we use the average absolute trajectory error (ATE RMSE[cm] \downarrow).

Implementation Details. Our method is implemented in Python using the PyTorch framework, incorporating CUDA for Gaussian Splatting, and trained on a desktop PC with NVIDIA RTX 3090Ti GPU. We extended the existing differentiable Gaussian Splatting rasterization code by adding functions to man-

Table 3: Camera tracking results on ScanNet datasets [3]. We use the ATE RMSE \downarrow [cm] as the metric and compare it with other SOTA methods.

Methods	Avg.	0000	0059	0106	0169	0181	0207
Vox-Fusion [40]	26.90	68.84	24.18	8.41	27.28	23.30	9.41
NICE-SLAM [45]	10.88	12.00	14.00	7.90	10.90	13.40	6.20
Co-SLAM [34]	8.72	7.35	11.45	9.68	6.03	11.93	8.86
ESLAM [11]	7.82	7.84	9.24	7.82	6.78	9.35	5.88
Point-SLAM [29]	12.19	10.24	7.81	8.65	22.16	14.77	9.54
SplaTAM [12]	11.88	12.83	10.10	17.72	12.08	11.10	7.46
Ours	10.84	11.28	9.24	16.49	11.09	10.88	6.58

age depth, pose, and cumulative opacity during both forward and backward propagation.

Baselines. The main baseline method we compare to is SplaTAM [12] as the representative of the GS-based SLAM systems because it is the only open-sourced GS-based SLAM system so far. Our method is also a plug-and-play method, which can improve the speed and memory usage for all GS-based methods. We also compared to other NeRF-based SLAM methods, such as NICE-SLAM [45], Co-SLAM [34], ESLAM [11], Vox-Fusion [40]. On the TUM-RGBD dataset, we also compare against three traditional SLAM systems: Kintinuous [35], Elastic-Fusion [36], and ORB-SLAM2 [25].

4.1 Experimental Results

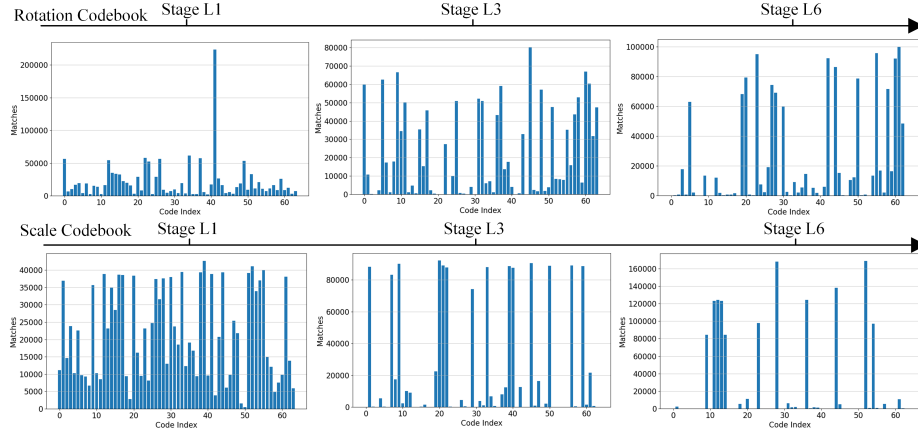
In this section, we present our experimental results on three different datasets. We evaluate the camera pose estimation, the 3D Gaussian reconstruction, and the real-time performance and memory usage of different SLAM systems.

Camera tracking results. In Tab. 2 3 4, we compare our method with other SOTA methods on camera pose estimation on different datasets. Best results are highlighted as **first**, **second**, and **third**. On the synthetic dataset Replica [30], we can see that we successfully reduce the trajectory error over the GS-based SLAM system (SplaTAM [12]) and achieve more accurate and robust pose estimation, shown in Tab. 2. The ScanNet dataset is a real-world dataset that has poor depth sensor information with high motion blur on RGB images. In Tab. 3, our method performs better than the GS-based SLAM system and similarly to the previous NeRF-based SLAM systems. In Tab. 4, we present the experimental results on TUM RGB-D datasets. We can see that our approach still outperforms other GS-based or NeRF-based methods, and the trajectory error has nearly 10% reduction. Our experiments demonstrate the effectiveness of our proposed reprojection loss, which can still improve the pose estimation accuracy with a number of Gaussian ellipsoids removed.

Gaussian reconstruction results. In Tab. 5, we show the rendering quality of the Replica dataset in 8 scenes. We also present the quantitative results in Fig. 6. Our method achieves similar PSNR, SSIM, and LPIPS results as SplaTAM [12]. Our approach achieves much better results than the NeRF-based baselines, such

Table 4: Camera tracking results on TUM RGB-D dataset [31]. We use the ATE RMSE \downarrow [cm] as the metric and compare it with other SOTA methods.

Methods	Avg.	fr1/desk	fr1/desk2	fr1/room	fr2/xyz	fr3/office
Kintinuous [35]	4.84	3.70	7.10	7.50	2.90	3.00
ElasticFusion [36]	6.91	2.53	6.83	21.49	1.17	2.52
ORB-SLAM2 [25]	1.98	1.60	2.20	4.70	0.40	1.00
NICE-SLAM [45]	15.87	4.26	4.99	34.49	31.73	3.87
Vox-Fusion [40]	11.31	3.52	6.00	19.53	1.49	26.01
Point-SLAM [29]	8.92	4.34	4.54	30.92	1.31	3.48
SplaTAM [12]	5.48	3.35	6.54	11.13	1.24	5.16
Ours	5.17	2.95	6.13	10.85	1.03	4.88

**Fig. 7:** We visualized the learned codebook indices for scale and rotation vector in the replica dataset. We can observe that as the stage progresses, the distribution of the codebook becomes increasingly compact. Due to the space limitation, we only visualize stages 1,3,6; the complete results are provided in the supplementary materials.

as Vox-Fusion [40], NICE-SLAM [45], Co-SLAM [34], and ESLAM [11]. Overall, our method can achieve better performance than the SOTA methods, while the speed and memory usage are significantly lower than other methods.

Real-time performance and memory usage. Tab. 6 illustrates the runtime performance and memory usage of our method and other GS-based and NeRF-based SLAM systems on the Replica [30] room 0 scene and the ScanNet [3] 0000 scene. We follow the settings of SplaTAM and use 60,90 iterations per frame for tracking and mapping to get similar performance in [12]. We evaluate the time consumption of tracking and mapping every iteration and every frame. Each iteration of our system renders a full 1200×980 pixel image (in Replica dataset) and 640×480 pixel image (in ScanNet dataset). Compared with the GS-based SLAM system, we significantly improve the training speed (**33%** faster), which is crucial for online SLAM systems, thanks to our compact 3D Gaussian scene presentation method. We also evaluate the rendering speed, the decoder parameters, and the memory of SOTA methods. Compared with the NeRF-based SLAM

Table 5: Quantitative image reconstruction performance on Replica dataset [30]. We use the PSNR \uparrow , SSIM \uparrow , and LPIPS \downarrow as the metrics and compare them with other SOTA methods.

Methods	Metrics	Avg.	R0	R1	R2	Of0	Of1	Of2	Of3	Of4
Vox-Fusion [40]	PSNR \uparrow	24.41	22.39	22.36	23.92	27.79	29.83	20.33	23.47	25.21
	SSIM \uparrow	0.80	0.68	0.68	0.80	0.86	0.88	0.79	0.80	0.85
	LPIPS \downarrow	0.24	0.30	0.30	0.23	0.24	0.18	0.24	0.21	0.20
Co-SLAM [34]	PSNR \uparrow	30.24	27.27	28.45	29.06	34.14	34.87	28.43	28.76	30.91
	SSIM \uparrow	0.94	0.91	0.91	0.93	0.96	0.97	0.94	0.94	0.96
	LPIPS \downarrow	0.25	0.32	0.29	0.27	0.21	0.20	0.26	0.23	0.24
ESLAM [11]	PSNR \uparrow	29.08	25.32	27.77	29.08	33.71	30.20	28.09	28.77	29.71
	SSIM \uparrow	0.93	0.86	0.90	0.93	0.96	0.92	0.94	0.95	0.95
	LPIPS \downarrow	0.25	0.31	0.30	0.25	0.18	0.23	0.24	0.20	0.20
NICE-SLAM [45]	PSNR \uparrow	24.42	22.12	22.47	24.52	29.07	30.34	19.66	22.23	24.49
	SSIM \uparrow	0.81	0.69	0.76	0.81	0.87	0.89	0.80	0.80	0.86
	LPIPS \downarrow	0.23	0.33	0.27	0.21	0.23	0.18	0.24	0.21	0.20
Point-SLAM [29]	PSNR \uparrow	35.17	32.40	34.08	35.50	38.26	39.16	33.99	33.48	33.49
	SSIM \uparrow	0.98	0.97	0.98	0.98	0.98	0.99	0.96	0.96	0.98
	LPIPS \downarrow	0.12	0.11	0.12	0.11	0.10	0.12	0.16	0.13	0.14
SplaTAM [12]	PSNR \uparrow	34.11	32.86	33.89	35.25	38.26	39.17	31.97	29.70	31.81
	SSIM \uparrow	0.97	0.98	0.97	0.98	0.98	0.97	0.97	0.95	0.95
	LPIPS \downarrow	0.10	0.07	0.10	0.08	0.09	0.09	0.10	0.12	0.15
Ours	PSNR \uparrow	34.44	32.98	34.08	35.35	38.16	39.07	32.37	31.08	32.31
	SSIM \uparrow	0.98	0.99	0.98	0.98	0.98	0.98	0.97	0.96	0.96
	LPIPS \downarrow	0.09	0.07	0.10	0.08	0.09	0.09	0.10	0.12	0.15

system, we achieve 414.45 FPS rendering speed on the replica dataset, which is **100 \times** significantly faster than these methods. Note that we do not use any neural network decoder in our system, which results in zero learnable parameters of the decoder. Compared with the GS-based SLAM system, our method also achieves **150%** reduction on memory usage and **176%** faster on rendering speed because of the proposed compact 3D Gaussian scene presentation.

4.2 Ablation Study

In this section, we conduct various experiments to verify the effectiveness of our method. Tab. 7 illustrates a quantitative evaluation with different settings on Replica [30] room0 scene.

Sliding window mask As shown in Tab. 7, the proposed sliding window mask effectively reduces the number of 3D Gaussian ellipsoids while retaining the image reconstruction performance. This demonstrates that we successfully remove the redundant and unessential 3D Gaussian ellipsoids created along with the SLAM system operation. Our mask strategy shows **50%** increase in the storage efficiency and a **26%** increase in rendering speed.

Residual vector codebook Our proposed geometry codebook method achieves a reduction in memory usage while maintaining the image reconstruction performance. We also present the scale and rotation codebook in different stages in

Table 6: Runtime and memory performance evaluation on Replica [30] and ScanNet [3] dataset. The De. Param denotes the parameter number of MLPs. The memory is the memory usage of the checkpoint.

	Method	Track/It.	Map/It.	Track/Fr.	Map/Fr.	Render FPS	De. Param.	Memory
Replica	NICE-SLAM	6.98ms	28.88ms	68.54ms	1.23s	0.30	0.06M	48.48MB
	ESLAM	6.85ms	19.98ms	54.80ms	0.29s	2.82	0.003M	27.12MB
	Co-SLAM	6.38ms	14.25ms	63.93ms	0.15s	3.68	0.013M	24.85MB
	Point-SLAM	0.57ms	34.85ms	22.72ms	10.47s	1.33	0.127M	55.42MB
	SplaTAM	25.43ms	23.8ms	2.25s	1.43s	125.64	0M	273.09MB
	Ours	18.37ms	17.48ms	1.53s	1.03s	347.73	0M	140.29MB
Scannet	NICE-SLAM	12.3ms	125.3ms	0.62s	7.52s	0.27	0.07M	84.25MB
	ESLAM	7.5ms	23.4ms	0.23s	0.70s	2.74	0.004M	67.9MB
	Co-SLAM	7.8ms	20.6ms	78ms	0.20s	3.41	0.015M	48.8MB
	Point-SLAM	0.63ms	42.29ms	64ms	12.69s	1.28	0.131M	27.8MB
	SplaTAM	29.22ms	27.27ms	2.63s	1.64s	115.48	0M	178.09MB
	Ours	21.91ms	20.25ms	1.99s	1.23s	328.93	0M	98.88MB

Table 7: The ablation study on Replica [30] dataset. We conduct experiments to verify the effectiveness of our method. Our full model achieves better pose estimation performance as well as faster training and rendering speed and lower memory usage.

Method	Accuracy				Real-time performance and Memory		
	PSNR	SSIM	LPIPS	ATE RMSE	Training Time	Render FPS	Memory
w/o mask	32.72	0.96	0.11	0.28	2.01H	245.28	243.09MB
w/o rvq	32.87	0.97	0.10	0.27	1.58H	272.29	178.88MB
w/o rep. loss	32.80	0.97	0.10	0.30	1.42H	347.73	140.29MB
Ours	32.98	0.98	0.09	0.27	1.42H	347.73	140.29MB

Fig. 7. As the stages progress, the magnitude of the codes diminishes, demonstrating that the residuals for each stage are being effectively trained to capture the geometry accurately.

Reprojection loss In Tab. 7, we can see that the proposed reprojection loss effectively improves the accuracy of camera pose estimation. As the 3D Gaussian represents the scene with a number of points, we use this reprojection loss to build the bridge of 3D points with 2D features, which can further improve the scene representation and the camera tracking accuracy.

5 Conclusion

In this paper, we propose a novel GS-based SLAM system with compact 3D Gaussian scene representation, reducing the number of redundant Gaussian ellipsoids without a decrease in performance. The proposed sliding window mask method and the geometry codebook improve the compactness of the scene representation, achieving faster training and rendering speed, and a significant reduction in memory usage. The proposed global bundle adjustment with reprojection loss further improves the camera tracking accuracy and scene representation. The extensive experiments demonstrate that our work provides a comprehensive

dense visual SLAM system, achieving high-fidelity performance, fast training, compactness, and real-time rendering.

References

1. Bengio, Y., Léonard, N., Courville, A.: Estimating or propagating gradients through stochastic neurons for conditional computation. *arXiv preprint arXiv:1308.3432* (2013) [6](#)
2. Cadena, C., Carlone, L., Carrillo, H., Latif, Y., Scaramuzza, D., Neira, J., Reid, I., Leonard, J.J.: Past, present, and future of simultaneous localization and mapping: Toward the robust-perception age. *IEEE Transactions on robotics* **32**(6), 1309–1332 (2016) [3](#)
3. Dai, A., Chang, A.X., Savva, M., Halber, M., Funkhouser, T., Niessner, M.: Scan-net: Richly-annotated 3d reconstructions of indoor scenes. In: *Proceedings of the IEEE Conference on Computer Vision and Pattern Recognition (CVPR)* (July 2017) [10](#), [11](#), [12](#), [14](#)
4. Deng, T., Liu, S., Wang, X., Liu, Y., Wang, D., Chen, W.: Prosgnerf: Progressive dynamic neural scene graph with frequency modulated auto-encoder in urban scenes. *arXiv preprint arXiv:2312.09076* (2023) [1](#)
5. Deng, T., Shen, G., Qin, T., Wang, J., Zhao, W., Wang, J., Wang, D., Chen, W.: Plgslam: Progressive neural scene representation with local to global bundle adjustment. *arXiv preprint arXiv:2312.09866* (2023) [1](#)
6. Deng, T., Xie, H., Wang, J., Chen, W.: Long-term visual simultaneous localization and mapping: Using a bayesian persistence filter-based global map prediction. *IEEE Robotics & Automation Magazine* **30**(1), 36–49 (2023) [1](#)
7. Durrant-Whyte, H., Bailey, T.: Simultaneous localization and mapping: part i. *IEEE robotics & automation magazine* **13**(2), 99–110 (2006) [1](#)
8. Défossez, A., Copet, J., Synnaeve, G., Adi, Y.: High fidelity neural audio compression. *arXiv preprint arXiv:2210.13438* (2022) [8](#)
9. Fan, Z., Wang, K., Wen, K., Zhu, Z., Xu, D., Wang, Z.: Lightgaussian: Unbounded 3d gaussian compression with 15x reduction and 200+ fps. *arXiv preprint arXiv:2311.17245* (2023) [6](#)
10. Izadi, S., Kim, D., Hilliges, O., Molyneaux, D., Newcombe, R., Kohli, P., Shotton, J., Hodges, S., Freeman, D., Davison, A., et al.: Kinectfusion: real-time 3d reconstruction and interaction using a moving depth camera. In: *Proceedings of the 24th annual ACM symposium on User interface software and technology*. pp. 559–568 (2011) [3](#)
11. Johari, M.M., Carta, C., Fleuret, F.: Eslam: Efficient dense slam system based on hybrid representation of signed distance fields. In: *Proceedings of the IEEE/CVF Conference on Computer Vision and Pattern Recognition*. pp. 17408–17419 (2023) [1](#), [4](#), [10](#), [11](#), [12](#), [13](#)
12. Keetha, N., Karhade, J., Jatavallabhula, K.M., Yang, G., Scherer, S., Ramanan, D., Luiten, J.: Splatam: Splat, track & map 3d gaussians for dense rgb-d slam. *arXiv preprint arXiv:2312.02126* (2023) [2](#), [4](#), [6](#), [9](#), [10](#), [11](#), [12](#), [13](#)
13. Kerbl, B., Kopanas, G., Leimkühler, T., Drettakis, G.: 3d gaussian splatting for real-time radiance field rendering. *ACM Transactions on Graphics* **42**(4) (2023) [2](#), [4](#), [9](#)
14. Kopanas, G., Philip, J., Leimkühler, T., Drettakis, G.: Point-based neural rendering with per-view optimization. In: *Computer Graphics Forum*. vol. 40, pp. 29–43. Wiley Online Library (2021) [5](#)

15. Kullback, S., Leibler, R.A.: On information and sufficiency. *The annals of mathematical statistics* **22**(1), 79–86 (1951) [7](#)
16. Lee, J.C., Rho, D., Sun, X., Ko, J.H., Park, E.: Compact 3d gaussian representation for radiance field. *arXiv preprint arXiv:2311.13681* (2023) [6](#)
17. Li, M., He, J., Jiang, G., Wang, H.: Ddn-slam: Real-time dense dynamic neural implicit slam with joint semantic encoding. *arXiv preprint arXiv:2401.01545* (2024) [4](#)
18. Li, M., Liu, S., Zhou, H.: Sgs-slam: Semantic gaussian splatting for neural dense slam. *arXiv preprint arXiv:2402.03246* (2024) [4](#)
19. Liu, J., Wang, G., Jiang, C., Liu, Z., Wang, H.: Translo: A window-based masked point transformer framework for large-scale lidar odometry. In: *Proceedings of the AAAI Conference on Artificial Intelligence*. vol. 37, pp. 1683–1691 (2023) [3](#)
20. Liu, J., Wang, G., Liu, Z., Jiang, C., Pollefeys, M., Wang, H.: Regformer: An efficient projection-aware transformer network for large-scale point cloud registration. In: *Proceedings of the IEEE/CVF International Conference on Computer Vision (ICCV)*. pp. 8451–8460 (October 2023) [3](#)
21. Matsuki, H., Murai, R., Kelly, P.H., Davison, A.J.: Gaussian splatting slam. *arXiv preprint arXiv:2312.06741* (2023) [2](#), [4](#)
22. Mildenhall, B., Srinivasan, P.P., Tancik, M., Barron, J.T., Ramamoorthi, R., Ng, R.: Nerf: Representing scenes as neural radiance fields for view synthesis. In: *ECCV* (2020) [1](#), [4](#)
23. Morgenstern, W., Barthel, F., Hilsmann, A., Eisert, P.: Compact 3d scene representation via self-organizing gaussian grids. *arXiv preprint arXiv:2312.13299* (2023) [6](#)
24. Mur-Artal, R., Montiel, J.M.M., Tardós, J.D.: Orb-slam: A versatile and accurate monocular slam system. *IEEE Transactions on Robotics* **31**(5), 1147–1163 (2015). <https://doi.org/10.1109/RO.2015.2463671> [1](#)
25. Mur-Artal, R., Tardós, J.D.: Orb-slam2: An open-source slam system for monocular, stereo, and rgb-d cameras. *IEEE Transactions on Robotics* **33**(5), 1255–1262 (2017). <https://doi.org/10.1109/RO.2017.2705103> [1](#), [9](#), [11](#), [12](#)
26. Newcombe, R.A., Lovegrove, S.J., Davison, A.J.: Dtam: Dense tracking and mapping in real-time. In: *2011 international conference on computer vision*. pp. 2320–2327. *IEEE* (2011) [1](#), [3](#)
27. Qin, T., Li, P., Shen, S.: Vins-mono: A robust and versatile monocular visual-inertial state estimator. *IEEE Transactions on Robotics* **34**(4), 1004–1020 (2018). <https://doi.org/10.1109/RO.2018.2853729> [1](#)
28. Reitmayr, G., Langlotz, T., Wagner, D., Mulloni, A., Schall, G., Schmalstieg, D., Pan, Q.: Simultaneous localization and mapping for augmented reality. In: *2010 International Symposium on Ubiquitous Virtual Reality*. pp. 5–8. *IEEE* (2010) [1](#)
29. Sandström, E., Li, Y., Van Gool, L., Oswald, M.R.: Point-slam: Dense neural point cloud-based slam. In: *Proceedings of the IEEE/CVF International Conference on Computer Vision*. pp. 18433–18444 (2023) [4](#), [10](#), [11](#), [12](#), [13](#)
30. Straub, J., Whelan, T., Ma, L., Chen, Y., Wijmans, E., Green, S., Engel, J.J., Mur-Artal, R., Ren, C., Verma, S., et al.: The replica dataset: A digital replica of indoor spaces. *arXiv preprint arXiv:1906.05797* (2019) [10](#), [11](#), [12](#), [13](#), [14](#)
31. Sturm, J., Engelhard, N., Endres, F., Burgard, W., Cremers, D.: A benchmark for the evaluation of rgb-d slam systems. In: *2012 IEEE/RSJ International Conference on Intelligent Robots and Systems*. pp. 573–580 (2012). <https://doi.org/10.1109/IRoS.2012.6385773> [10](#), [12](#)
32. Sucar, E., Liu, S., Ortiz, J., Davison, A.J.: imap: Implicit mapping and positioning in real-time. In: *ICCV*. pp. 6229–6238 (October 2021) [1](#), [4](#)

33. Teed, Z., Deng, J.: Droid-slam: Deep visual slam for monocular, stereo, and rgb-d cameras. *Advances in neural information processing systems* **34**, 16558–16569 (2021) [4](#)
34. Wang, H., Wang, J., Agapito, L.: Co-slam: Joint coordinate and sparse parametric encodings for neural real-time slam. In: *Proceedings of the IEEE/CVF Conference on Computer Vision and Pattern Recognition*. pp. 13293–13302 (2023) [1](#), [4](#), [10](#), [11](#), [12](#), [13](#)
35. Whelan, T., Kaess, M., Johannsson, H., Fallon, M., Leonard, J.J., McDonald, J.: Real-time large-scale dense rgb-d slam with volumetric fusion. *The International Journal of Robotics Research* **34**(4-5), 598–626 (2015) [1](#), [11](#), [12](#)
36. Whelan, T., Salas-Moreno, R.F., Glocker, B., Davison, A.J., Leutenegger, S.: Elasticfusion: Real-time dense slam and light source estimation. *The International Journal of Robotics Research* **35**(14), 1697–1716 (2016) [1](#), [11](#), [12](#)
37. Xie, H., Deng, T., Wang, J., Chen, W.: Robust incremental long-term visual topological localization in changing environments. *IEEE Transactions on Instrumentation and Measurement* **72**, 1–14 (2022) [1](#)
38. Xie, H., Deng, T., Wang, J., Chen, W.: Angular tracking consistency guided fast feature association for visual-inertial slam. *IEEE Transactions on Instrumentation and Measurement* (2024) [1](#)
39. Yan, C., Qu, D., Wang, D., Xu, D., Wang, Z., Zhao, B., Li, X.: Gs-slam: Dense visual slam with 3d gaussian splatting. *arXiv preprint arXiv:2311.11700* (2023) [2](#), [4](#), [6](#)
40. Yang, X., Li, H., Zhai, H., Ming, Y., Liu, Y., Zhang, G.: Vox-fusion: Dense tracking and mapping with voxel-based neural implicit representation. In: *2022 IEEE International Symposium on Mixed and Augmented Reality (ISMAR)*. pp. 499–507 (2022). <https://doi.org/10.1109/ISMAR55827.2022.00066> [4](#), [10](#), [11](#), [12](#), [13](#)
41. Yifan, W., Serena, F., Wu, S., Öztireli, C., Sorkine-Hornung, O.: Differentiable surface splatting for point-based geometry processing. *ACM Transactions on Graphics (TOG)* **38**(6), 1–14 (2019) [5](#)
42. Yugay, V., Li, Y., Gevers, T., Oswald, M.R.: Gaussian-slam: Photo-realistic dense slam with gaussian splatting. *arXiv preprint arXiv:2312.10070* (2023) [2](#), [4](#)
43. Zeghidour, N., Luebs, A., Omran, A., Skoglund, J., Tagliasacchi, M.: Soundstream: An end-to-end neural audio codec. *IEEE/ACM Transactions on Audio, Speech, and Language Processing* **30**, 495–507 (2021) [8](#)
44. Zhu, S., Wang, G., Blum, H., Liu, J., Song, L., Pollefeys, M., Wang, H.: Sni-slam: Semantic neural implicit slam. *arXiv preprint arXiv:2311.11016* (2023) [4](#)
45. Zhu, Z., Peng, S., Larsson, V., Xu, W., Bao, H., Cui, Z., Oswald, M.R., Pollefeys, M.: Nice-slam: Neural implicit scalable encoding for slam. In: *CVPR*. pp. 12786–12796 (June 2022) [1](#), [4](#), [10](#), [11](#), [12](#), [13](#)